

# Model-based T1, T2\* and Proton Density Mapping Using a Bayesian Approach with Parameter Estimation and Complementary Undersampling Patterns

Shuai Huang<sup>1</sup>, James J. Lah<sup>2</sup>, Jason W. Allen<sup>1,2</sup>, and Deqiang Qiu\*<sup>1</sup>

<sup>1</sup>Department of Radiology and Imaging Sciences, Emory University, Atlanta, GA, 30322, USA

<sup>2</sup>Department of Neurology, Emory University, Atlanta, GA, 30322, USA

Word Count for the body of the text: 4772.

---

\*This work is supported by National Institutes of Health under Grants R21AG064405, R01AG072603, R01AG070937 and P30AG066511. Corresponding author: Deqiang Qiu (deqiang.qiu@emory.edu).

## Abstract

**Purpose:** To achieve automatic hyperparameter estimation for the joint recovery of quantitative MR images, we propose a Bayesian formulation of the reconstruction problem that incorporates the signal model. Additionally, we investigate the use of complementary undersampling patterns to determine optimal undersampling schemes for quantitative MRI.

**Theory:** We introduce a novel nonlinear approximate message passing framework, referred to as “AMP-PE”, that enables the simultaneous recovery of distribution parameters and quantitative maps.

**Methods:** We employed the variable flip angle multi-echo (VFA-ME) method to acquire measurements. Both retrospective and prospective undersampling approaches were utilized to obtain Fourier measurements using variable-density and Poisson-disk patterns. Furthermore, we extensively explored various undersampling schemes, incorporating complementary patterns across different flip angles and/or echo times.

**Results:** AMP-PE adopts a model-based joint recovery strategy, it outperforms the  $l_1$ -norm minimization approach that follows a decoupled recovery strategy. A comparison with an existing joint-recovery approach further demonstrates the advantageous outcomes of AMP-PE. For quantitative  $T_1$  mapping using VFA-ME, employing identical k-space sampling patterns across different echo times produced the best performance. Whereas for  $T_2^*$  and proton density mappings, using complementary sampling patterns across different flip angles yielded the best performance.

**Conclusion:** AMP-PE is equipped with built-in parameter estimation, and works naturally in clinical settings with varying acquisition protocols and scanners. It also achieves improved performance by combining information from the MR signal model and the sparse prior on images.

**Keywords:** Approximate message passing, Compressive sensing, Quantitative MRI, Hyperparameter estimation, Variable flip angle, Multi-echo, Complementary undersampling pattern, Variable density, Poisson disc.

# 1 Introduction

Quantitative MRI (qMRI) techniques are used to measure important tissue parameters, including the  $T_1$ ,  $T_2$ , and  $T_2^*$  relaxation times and proton density. These quantitative maps have proven valuable in detecting subtle changes in tissue properties, and have gained significant traction as potential biomarkers for investigating age-related neurodegenerative diseases [1–6]. Nevertheless, acquiring a fully-sampled dataset in the  $k$ -space for high-resolution 3D volumetric scans can be time-consuming, leading to patient discomfort and the potential introduction of motion artifacts in reconstructed images. To mitigate this, undersampling techniques are commonly employed to reduce scan time, albeit at the cost of decreased image quality. Consequently, it becomes crucial to incorporate additional prior information into the image reconstruction process to enhance the overall image quality.

First, natural images are widely acknowledged to have sparse representations. Specifically, most of the image wavelet coefficients are close to zero, with the energy concentrated in only a few significant entries. Compressive sensing (CS) leverages this sparsity property and encourages sparse solutions in a suitable basis, such as the wavelet basis [7–9]. Various methods, including regularization and Bayesian approaches, have been proposed to enforce the sparse prior on image wavelet coefficients [10–15], and we also employ this approach in this paper to enhance image quality.

Second, MR signals are governed by the Bloch equation that includes the underlying tissue parameters and MR acquisition parameters. The inherent correlation among different MR images of the same subject indicates a shared joint sparse and/or low-rank structure, which has been harnessed to achieve improved reconstruction performance [16–22]. Alternatively, the signal model can be directly employed as a prior and integrated into the reconstruction process. This gives rise to a range of model-based joint recovery strategies that offer enhanced performance [23–34]. However, a key challenge faced by these joint approaches is the determination of multiple regularization or constraint parameters for optimal results. Manual hyperparameter tuning becomes increasingly cumbersome as the number of images in the model grows, and the process needs to be repeated for various MR scanners or protocols. To tackle this issue, we adopt a Bayesian perspective and employ approximate message passing (AMP) to automatically estimate hyperparameters in this paper.

AMP has gained wide recognition and utilization in sparse signal recovery due to its efficiency and state-of-the-art performance [12, 13, 35–40]. However, the standard AMP was originally developed for linear systems [13, 35], it cannot be used to recover MR tissue parameters in the nonlinear signal model. AMP has been used to recover MR images from linear  $k$ -space measurements [41–43]. Rich et al. later designed a nonlinear AMP framework for phase-contrast MRI and 4D flow imaging [44–46]. In this study, we propose an extension to the AMP framework specifically tailored for the nonlinear recovery of MR tissue parameters. In contrast to standard regularization or constraint approaches that necessitate hyperparameter tuning, AMP enables the simultaneous recovery of the

signal and hyperparameters in an automatic and adaptive manner. This characteristic renders it an ideal choice for clinical settings involving different scanners and acquisition protocols. We have previously applied this framework to the recovery of  $T_2^*$  and phase images [47]. In this paper, we further extend our approach to jointly recover  $T_1$ ,  $T_2^*$ , and proton density maps while additionally comparing various undersampling strategies.

Popular options for undersampling patterns include the variable-density pattern [48], Poisson-disk pattern [49], among others. To achieve maximum coverage of the k-space, complementary patterns can be adopted at various flip angles and echo times [23, 50–54]. While previous studies have commonly employed complementary patterns at all flip angles and echo times to enhance multi-contrast MRI, our findings demonstrate that this approach does not hold for quantitative MRI. Specifically, for  $T_1$  mapping using VFA-ME, it is advantageous to use identical sampling patterns across different echo times. Conversely, for  $T_2^*$  and proton density mappings, employing complementary sampling patterns across different flip angles yields better results.

## 2 Theory

Variable-flip-angle (VFA) 3D gradient-echo (GRE) has emerged as a popular technique for quantitative MR imaging [55, 56]. The acquired measurements span multiple flip angles and echo times. Using the GRE sequence, we acquire undersampled Fourier measurements  $\mathbf{y}_{ij} \in \mathbb{C}^M$  of VFA multi-echo images  $\mathbf{z}_{ij} \in \mathbb{C}^N$  at the  $i$ -th flip angle  $\theta_i$  and  $j$ -th echo time  $t_j$ :

$$\mathbf{y}_{ij} = \mathbf{A}_{ij}\mathbf{z}_{ij} + \mathbf{w}_{ij}, \quad (1)$$

where  $i \in \{1, \dots, I\}$ ,  $j \in \{1, \dots, J\}$ ,  $\mathbf{A}_{ij}$  is the measurement matrix, and  $\mathbf{w}_{ij}$  is the measurement noise. The collection of measurements across all flip angles and echo times is denoted by  $\mathbf{y} \in \mathbb{C}^{MIJ}$ . The wavelet coefficients  $\mathbf{v}_{ij}$  of the image  $\mathbf{z}_{ij}$  are mostly close to zero, i.e. approximately sparse, in the wavelet domain:

$$\mathbf{v}_{ij} = \mathbf{H}\mathbf{z}_{ij}, \quad (2)$$

where  $\mathbf{H}$  is the invertible wavelet transform matrix. The sparse prior on  $\mathbf{v}_{ij}$  is widely used to enhance the quality of reconstructed images [57].

Assuming a longitudinal steady-state can be reached with perfect spoiling, the magnitude of the complex MR signal  $z_{ij}$  from a spoiled GRE sequence can be expressed as [58]

$$\begin{aligned} |z_{ij}| &= f_{ij}(z_0, t_1, t_2^*) \\ &= z_0 \cdot \sin \theta_i \cdot \frac{1 - \exp(-TR/t_1)}{1 - \cos \theta_i \cdot \exp(-TR/t_1)} \cdot \exp(-t_j/t_2^*), \end{aligned} \quad (3)$$

where  $z_0$  is the proton density,  $t_1$  is the  $T_1$  relaxation time,  $t_2^*$  is the  $T_2^*$  relaxation time,  $TR$  is the repetition time.

Utilizing the sparse prior on image wavelet coefficients  $\mathbf{z}_{ij}$ , we first calculate the posterior distribution  $p_s(\mathbf{v}_{ij}|\mathbf{y})$  of the VFA multi-echo image  $\mathbf{v}_{ij}$  from a probabilistic perspective. Subsequently, we consider this distribution,  $p_s(\mathbf{v}_{ij}|\mathbf{y})$ , as the prior for the VFA multi-echo image  $\mathbf{v}_{ij}$  and integrate it with the signal model prior for a joint reconstruction of the  $T_1$ ,  $T_2^*$ , and proton density maps.

## 2.1 VFA Multi-echo Image Prior

We first model the distribution of wavelet coefficients  $\mathbf{v}_{ij}$  using the Laplace distribution. These wavelet coefficients are assumed to be independent and identically distributed (i.i.d.):

$$p(v | \lambda) = \frac{1}{2} \lambda \cdot \exp(-\lambda|v|), \quad (4)$$

where  $\lambda > 0$  is the unknown distribution parameter.

We then model the noise distribution using the complex additive white-Gaussian distribution:

$$p(w | \tau_w) = \frac{1}{\pi \tau_w} \exp\left(-\frac{|w|^2}{\tau_w}\right), \quad (5)$$

where  $\tau_w$  is the noise variance.

Within the AMP framework, the distribution parameters  $\lambda_{ij}, \tau_w$  are treated as unknown variables [14]. The factor graph for the forward model (1) is illustrated in Fig. 1a, where variable nodes are denoted by “○” and contain random variables. The factor nodes, represented by “■”, encode the probability distributions of these random variables. In particular, the factor nodes  $\Omega_{ijn}$  and  $\Phi_{ijm}$  correspond to the signal and noise priors, respectively.

$$\Omega_{ijn}(v_{ijn}, \lambda_{ij}) = p(v_{ijn} | \lambda_{ij}) \quad (6)$$

$$\Phi_{ijm}(y_{ijm}, \mathbf{v}_{ij}, \tau_w) = p(y_{ijm} - \mathbf{b}_{ijm} \mathbf{v}_{ij} | \tau_w), \quad (7)$$

where  $\mathbf{b}_{ijm}$  is the  $m$ -th row of the measurement matrix  $\mathbf{B}_{ij} = \mathbf{A}_{ij} \mathbf{H}^{-1}$ .

Messages about the variable distributions are passed and discussed among the factor nodes until a consensus is reached. As an example, we use the following notations to denote the messages passed between the  $n$ -th variable node  $v_{ijn}$  and the  $m$ -th factor node  $\Phi_{ijm}$  (at the  $i$ -th flip angle and  $j$ -th echo):

- $\Delta_{v_{ijn} \rightarrow \Phi_{ijm}}$  denotes the message from  $v_{ijn}$  to  $\Phi_{ijm}$ ,
- $\Delta_{\Phi_{ijm} \rightarrow v_{ijn}}$  denotes the message from  $\Phi_{ijm}$  to  $v_{ijn}$ ,

where  $n \in \{1, \dots, N\}$  and  $m \in \{1, \dots, M\}$ . Both  $\Delta_{v_{ijn} \rightarrow \Phi_{ijm}}$  and  $\Delta_{\Phi_{ijm} \rightarrow v_{ijn}}$  are functions of the variable  $v_{ijn}$ , and they are expressed in the “log” domain in this paper. The derivation of the AMP algorithm falls beyond the scope of this paper, and algorithmic details can be found in [13, 14]. For readers’ convenience, a detailed introduction to AMP is provided in Section S-I of the Supporting Information.

Drawing upon the graphical model theory [59], the posterior distribution of a variable is proportional to the exponential function of the sum of messages passed to that variable:

$$p(\lambda_{ij}|\mathbf{y}) \propto \exp\left(\sum_n \Delta_{\Psi_{ijn} \rightarrow \lambda_{ij}}\right) \quad (8)$$

$$p(\tau_w|\mathbf{y}) \propto \exp\left(\sum_{ijm} \Delta_{\Phi_{ijm} \rightarrow \tau_w}\right) \quad (9)$$

$$p(v_{ijn}|\mathbf{y}) \propto \exp\left(\Delta_{\Psi_{ijn} \rightarrow v_{ijn}} + \sum_m \Delta_{\Phi_{ijm} \rightarrow v_{ijn}}\right). \quad (10)$$

We can then estimate the distribution parameters  $\{\lambda_{ij}, \tau_w\}$  using their maximum-a-posteriori (MAP) estimations

$$\hat{\lambda}_{ij} = \arg \max_{\lambda_{ij}} p(\lambda_{ij}|\mathbf{y}) \quad (11)$$

$$\hat{\tau}_w = \arg \max_{\tau_w} p(\tau_w|\mathbf{y}). \quad (12)$$

To achieve accurate parameter estimation, it is essential to compute the distributions  $p(\lambda_{ij}|\mathbf{y})$  and  $p(\tau_w|\mathbf{y})$  exactly. However, in the AMP framework, the distribution  $p(v_{ijn}|\mathbf{y})$  can be ‘‘approximated’’ by a Gaussian distribution to simplify the calculations without sacrificing accuracy [60]:

$$p(v_{ijn}|\mathbf{y}) \approx \mathcal{CN}\left(v_{ijn} \mid \mu_{(v_{ijn})}, \kappa_{(v_{ijn})}\right), \quad (13)$$

where  $\mathcal{CN}(\cdot)$  is the complex Gaussian density function,  $\mu_{(v_{ijn})}$  and  $\kappa_{(v_{ijn})}$  are the corresponding mean and variance of the wavelet coefficient  $v_{ijn}$ . Since the wavelet transform  $\mathbf{v} = \mathbf{H}\mathbf{z}$  is invertible, we can compute the posterior distribution of the VFA multi-echo image  $\mathbf{z}_{ij}$  from that of the wavelet coefficients  $\mathbf{v}_{ij}$  in (13) straightforwardly:

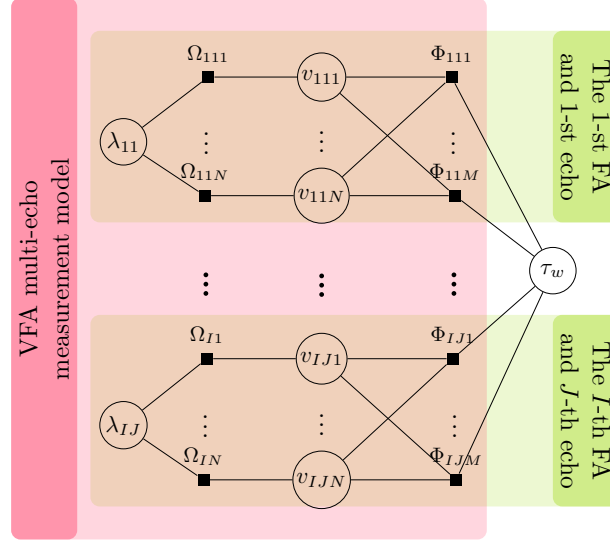
$$p_s(z_{ijn}|\mathbf{y}) \approx \mathcal{CN}\left(z_{ijn} \mid \mu_{s(z_{ijn})}, \kappa_{s(z_{ijn})}\right), \quad (14)$$

where  $\mu_{s(z_{ijn})}$  and  $\kappa_{s(z_{ijn})}$  are the corresponding mean and variance of the  $n$ -th image voxel  $z_{ijn}$ . The distribution  $p_s(z_{ijn}|\mathbf{y})$  serves as the VFA multi-echo image prior and is combined with the signal model prior in our proposed nonlinear AMP framework.

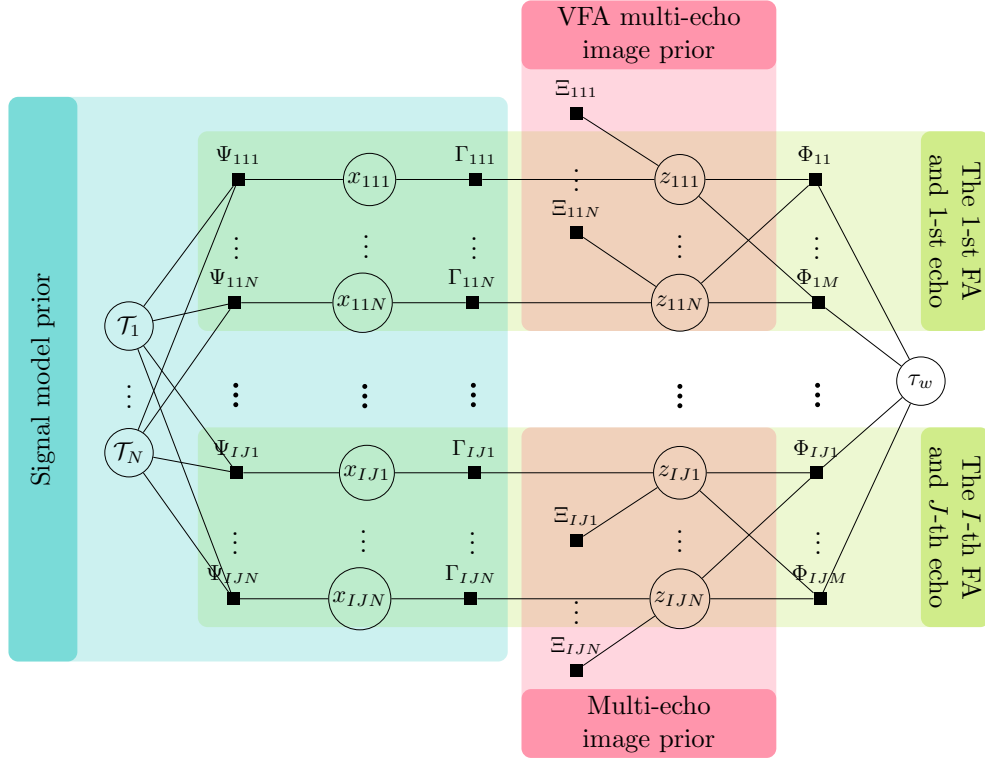
## 2.2 Proposed Nonlinear AMP framework

The factor graph of the proposed nonlinear AMP framework for reconstructing the tissue parameters is shown in Fig. 1b. We shall introduce a new variable  $x_{ijn}$  to represent the MR signal magnitude. It is connected to the complex MR signal  $z_{ijn}$  through the factor node  $\Gamma_{ijn}$ :

$$\Gamma_{ijn}(x_{ijn}, z_{ijn}) = \delta(x_{ijn} - |z_{ijn}|), \quad (15)$$



(a)



(b)

Figure 1: (a) The factor graph used to compute the VFA multi-echo image prior  $p_s(\mathbf{z}_{ijn}|\mathbf{y})$  from the measurement model in (1). (b) The factor graph used to recover the tissue parameters  $\mathcal{T}_n = \{z_0(n), t_1(n), t_2^*(n)\}$  by combining the VFA multi-echo image prior with the signal model prior in (3).

where  $\delta(\cdot)$  is the Dirac impulse. The VFA multi-echo image prior and the signal model prior are encoded in the factor nodes  $\Xi_{ijn}$  and  $\Psi_{ijn}$  respectively:

$$\Xi_{ijn}(z_{ijn}) = p_s(z_{ijn}|\mathbf{y}) \quad (16)$$

$$\Psi_{ijn}(x_{ijn}, z_0(n), t_1(n), t_2^*(n)) = \delta(x_{ijn} - f_{ij}(z_0(n), t_1(n), t_2^*(n))), \quad (17)$$

where  $f_{ij}(\cdot)$  is the signal model in (3).

To simplify the discussion, we narrow our focus to the message passing steps between  $\{z_{ijn}\}$  and the tissue parameters  $\mathcal{T}_n = \{z_0(n), t_1(n), t_2^*(n)\}$  on the factor graph depicted in Fig. 1b. In this context, we integrate the VFA multi-echo image prior with the signal model prior. The message passing proceeds sequentially through the variable and factor nodes connecting  $\{z_{ijn}\}$  and  $\mathcal{T}_n$ . We then have:

1) **Message passing from  $\{z_{ijn}\}$  to  $\mathcal{T}_n$ .**

The messages proceed as follows:

$$\Delta_{z_{ijn} \rightarrow \Gamma_{ijn}} \Rightarrow \Delta_{\Gamma_{ijn} \rightarrow x_{ijn}} \Rightarrow \Delta_{\Gamma_{ijn} \rightarrow x_{ijn}} \Rightarrow \Delta_{x_{ijn} \rightarrow \Psi_{ijn}} \Rightarrow \Delta_{\Psi_{ijn} \rightarrow \mathcal{T}_n}. \quad (18)$$

From the factor graph in Fig. 1b, we can see that the message  $\Delta_{z_{ijn} \rightarrow \Gamma_{ijn}}$  is a combination of the messages from  $\Phi_{ijm}$  and  $\Xi_{ijn}$ . Since the distributions of  $\{\mathbf{v}_{ij}, \mathbf{z}_{ij}\}$  are approximated by Gaussian distributions in AMP [13, 60], the message  $\Delta_{z_{ijn} \rightarrow \Gamma_{ijn}}$  can also be approximated by the logarithm of a Gaussian density function:

$$\begin{aligned} \Delta_{z_{ijn} \rightarrow \Gamma_{ijn}} &= \sum_m \Delta_{\Phi_{ijm} \rightarrow z_{ijn}} + \log \Xi_{ijn}(z_{ijn}) \\ &= -\frac{1}{\pi \tau_1(z_{ijn})} \left| z_{ijn} - \mu_1(z_{ijn}) \right|^2 + C, \end{aligned} \quad (19)$$

where  $\mu_1(z_{ijn})$ ,  $\tau_1(z_{ijn})$  are the corresponding mean and variance of the entry  $z_{ijn}$ ,  $C$  is a normalizing constant.

The detailed expressions of the rest messages in (18) are derived in a similar fashion in Appendix A. Combining the messages from all the factor nodes  $\{\Psi_{ijn}\}$  connected to  $\mathcal{T}_n$ , we can calculate the posterior distribution of the tissue parameters  $\mathcal{T}_n$  as follows:

$$p(\mathcal{T}_n|\mathbf{y}) \propto \exp \left( \sum_{ij} \Delta_{\Psi_{ijn} \rightarrow \mathcal{T}_n} \right) \quad (20)$$

To enhance stability, AMP typically enforces the variances  $\{\tau_1(z_{ijn})\}$  in (19) to be the same



across all the entries in  $z_{ij}$ . The MAP estimations of the tissue parameters are then

$$\begin{aligned}\widehat{\mathcal{T}}_n &= \arg \max_{\mathcal{T}_n} p(\mathcal{T}_n | \mathbf{y}) \\ &= \arg \min_{\mathcal{T}_n} \sum_{ij} \left( f_{ij}(z_0(n), t_1(n), t_2^*(n)) - \left| \mu_{1(z_{ijn})} \right| \right)^2.\end{aligned}\quad (21)$$

The above (21) is a nonlinear least-squares fitting problem, it can be decomposed into three one-dimensional problems with respect to  $z_0(n)$ ,  $t_1(n)$ ,  $t_2^*(n)$ . The optimization with respect to  $z_0(n)$  is convex, and can be solved easily. While the optimizations involving  $t_1(n)$  and  $t_2^*(n)$  are nonconvex, they can still be efficiently solved using a dictionary-based exhaustive search approach, once the search intervals are properly defined.

## 2) Message passing from $\mathcal{T}_n$ to $\{z_{ijn}\}$ .

The messages proceed as follows:

$$\Delta_{\Psi_{ijn} \rightarrow x_{ijn}} \Rightarrow \Delta_{x_{ijn} \rightarrow \Gamma_{ijn}} \Rightarrow \Delta_{\Gamma_{ijn} \rightarrow z_{ijn}}. \quad (22)$$

The detailed expressions of the above messages are also given in Appendix A. Combining the messages from  $\Gamma_{ijn}$ ,  $\{\Phi_{ijm}\}$  and the VFA multi-echo image prior  $\Xi_{ijn}$ , we can finally calculate the posterior distribution of  $z_{ijn}$  as follows:

$$p(z_{ijn} | \mathbf{y}) \propto \exp \left( \Delta_{\Gamma_{ijn} \rightarrow z_{ijn}} + \log \Xi_{ijn}(z_{ijn}) + \sum_m \Delta_{\Phi_{ijm} \rightarrow z_{ijn}} \right). \quad (23)$$

The rest message passing steps between  $z_{ijn}$  and  $\tau_w$  are the same as the conventional linear AMP discussed in [13] (see Section S-I of the Supporting Information). As mentioned earlier, the message passing process will be performed iteratively until the convergence is reached. The recovered tissue parameters  $\widehat{\mathcal{T}}_n$  are given by their MAP estimations in (21).

## 3 Methods

We collected *in vivo* 3D brain data using a 3T MRI scanner (Prisma model, Siemens Healthcare, Erlangen, Germany), after obtaining written consent from the subjects and receiving approval from the Institutional Review Board of Emory University. The data were acquired using a 32-channel head coil and the GRE sequence. Our objective was to reduce the scan time to approximately 10 minutes, which led us to explore the low-sampling-rate regime, where the undersampling rates varied among 10%, 15%, 20%. Both retrospective and prospective undersampling schemes were implemented in our experiments. In the retrospective scheme, a fully-sampled dataset was acquired during the scan and then retrospectively undersampled. The reconstructions from the fully-sampled data were used as the ground-truth reference images for comparing different approaches. On the other hand, the prospective scheme involved real-time acquisition of the undersampled dataset.

Since it lacked the reference images, its purpose was to validate the feasibility of performing undersampling in a clinical setting.

**Retrospective Undersampling:** The k-space was fully sampled during the scan within an elliptical region of the  $y - z$  plane, as illustrated in Fig. 2a. Subsequently, retrospective undersampling was performed in the  $y - z$  plane using the undersampling patterns shown in Fig. 2a, while the readout  $x$ -direction was always fully sampled. For the estimation of sensitivity maps via ESPIRiT [61], the central  $24 \times 24$  k-space was fully sampled. We employed variable-density and Poisson-disk undersampling patterns and compared their performances. Six subjects, denoted as “R0–R5”, were recruited for the study. Among them, one subject “R0” was randomly chosen as the training dataset (for approaches that required parameter-tuning), while the remaining subjects “R1–R5” served as the test dataset. The acquisition parameters were as follows

- We included three flip angles =  $5^\circ$ ,  $10^\circ$ ,  $20^\circ$ ; the number of echoes = 4, the first echo time = 7 ms, echo spacing = 8 ms; TR = 36 ms; the number of slices = 96, slice thickness = 1.5 mm; FOV = 256 mm  $\times$  232 mm, in-plane resolution = 1 mm  $\times$  1 mm, bandwidth per pixel = 260 Hz. The acquisition time was 32.83 minutes.

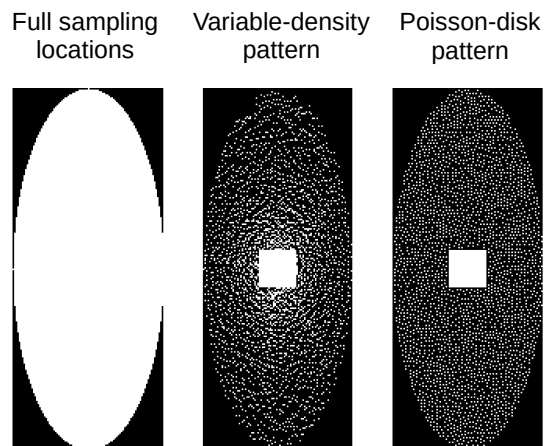
**Prospective Undersampling:** The prospective protocols were implemented via pulse sequence programming using the “IDEA” platform from Siemens. The undersampling took place in the  $y - z$  plane in real time, and the readout  $x$ -direction was always fully sampled. Five subjects, denoted as “P1–P5”, were recruited for this study. The acquisition parameters were as follows

- We included three flip angles =  $5^\circ$ ,  $10^\circ$ ,  $20^\circ$ ; the number of echoes = 4, the first echo time = 7 ms, echo spacing = 8 ms; TR = 36 ms; the number of slices = 96, slice thickness = 1.5 mm; FOV = 256 mm  $\times$  232 mm, in-plane resolution = 1 mm  $\times$  1 mm, bandwidth per pixel = 260 Hz. When the undersampling rates vary in  $\{10\%, 15\%, 20\%\}$ , the acquisition times were 5.43, 7.43 and 9.43 minutes respectively.

The double-flip angle method was employed to measure B1 transmit (B1+) field using a echo planar imaging sequence [62]. The obtained B1+ field was then combined with Bloch-simulation of the slice-profile of the slab-selective radio-frequency pulse in the 3D GRE sequence to calculate a spatially resolved flip-angle map.

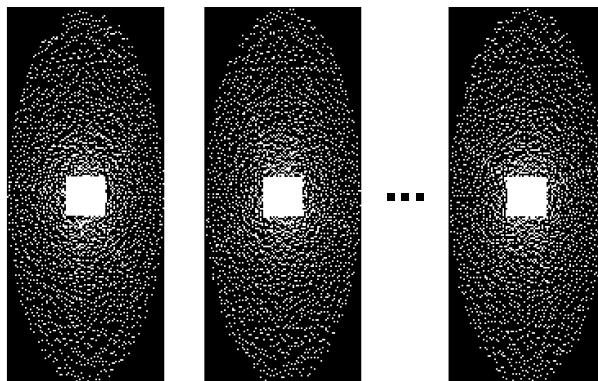
With retrospective undersampling, we investigated the use of complementary undersampling patterns shown in Fig. 2b for data acquisition through the following undersampling schemes:

- 1)  $U1$ : The sampling patterns are complementary across different flip angles and echo times.
- 2)  $U2$ : The sampling patterns are complementary across different flip angles, but the same across different echo times.
- 3)  $U3$ : The sampling patterns are the same across different flip angles, but complementary across different echo times.

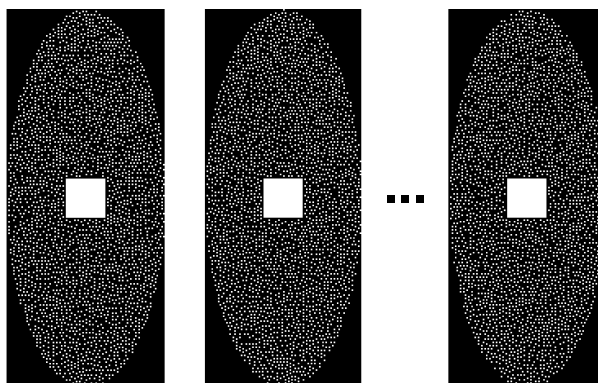


(a)

Complementary variable-density patterns



Complementary Poisson-disk patterns



(b)

Figure 2: (a) Variable-density and Poisson-disk patterns are two popular undersampling patterns. (b) Complementary undersampling patterns can be adopted across different flip angles and echo times to increase the coverage of  $k$ -space.

- 4)  $U_4$ : The sampling patterns are the same across different flip angles and echo times.

After the best undersampling schemes for reconstruction were determined, we applied them in prospective undersampling.

The Daubechies wavelet family was chosen to obtain the sparse representation of an image [9]. The orthogonal “db1-db10” wavelet bases are commonly used, with the complexity of the basis increasing with its order. For the reconstructions of  $R_2^*$  map and QSM [47], it was observed that employing a higher-order wavelet basis generally resulted in improved image quality. In our experiments, we utilized the db6 basis with 4 levels to strike a balance between wavelet complexity and image quality.

### 3.1 Comparison with the Least Squares and $l_1$ -norm Regularization Approaches

We first conducted a comparison between the proposed “AMP with built-in parameter estimation” (AMP-PE) approach and the baseline least squares (LSQ) approach, as well as the state-of-the-art  $l_1$ -norm regularization (L1) approach [57].

- The least squares approach:

$$\min_{z_{ij}} \|y_{ij} - \mathbf{A}_{ij} z_{ij}\|_2^2 \tag{24a}$$

$$\min_{z_0, t_1, t_2^*} \sum_{ij} (f_{ij}(z_0, t_1, t_2^*) - |z_{ij}|)^2 . \tag{24b}$$

The least squares approach does not require parameter tuning, and the solutions can be obtained using gradient descent. Specifically, the recovery of  $z_0$ ,  $t_1$ , and  $t_2^*$  is performed sequentially until convergence. As mentioned earlier, the recovery of  $z_0$  is a convex problem and can be easily solved. On the other hand, the recovery of  $t_1$  and  $t_2^*$  is a nonconvex problem, but it can still be efficiently solved through exhaustive search within the predefined intervals.

- The  $l_1$ -norm regularization approach:

$$\min_{v_{ij}} \|y_{ij} - \mathbf{B}_{ij} v_{ij}\|_2^2 + \kappa \cdot \|v_{ij}\|_1 \tag{25a}$$

$$\min_{z_0, t_1, t_2^*} \sum_{ij} (f_{ij}(z_0, t_1, t_2^*) - |z_{ij}|)^2 , \tag{25b}$$

where  $\mathbf{B}_{ij} = \mathbf{A}_{ij} \mathbf{H}^{-1}$ ,  $\kappa$  is the regularization parameter. The  $l_1$ -norm of the wavelet coefficients was employed as the regularizer to encourage sparse solutions. The parameter  $\kappa = 5e-2$  was tuned on the training dataset “R0” to achieve optimal performance. We utilized the Fast Iterative Shrinkage-Thresholding Algorithm (FISTA) to solve (25a) [63]. The recovery of  $z_0$ ,  $t_1$ , and  $t_2^*$  was also carried out sequentially until convergence.

- In the proposed AMP-PE approach, when the undersampling rate is low, the damping operation is necessary to stabilize the AMP update of the wavelet coefficients  $\mathbf{v}$  [64]. Let  $\mu_d^{(t)}(v)$

denote the damped solution in the previous  $t$ -th iteration, and  $\mu^{(t+1)}(v)$  denote the undamped solution in the  $(t + 1)$ -th iteration. The damping operation simply proceeds as follows:

$$\mu_{(z_{ijn})}^{(t+1)}(d) = \mu_{(z_{ijn})}^{(t)}(d) + \alpha \cdot \left( \mu_{(z_{ijn})}^{(t+1)} - \mu_{(z_{ijn})}^{(t)}(d) \right), \quad (26)$$

where  $\alpha \in (0, 1]$  is the damping rate,  $\mu_{(z_{ijn})}^{(t+1)}(d)$  is the damped solution in the  $(t + 1)$ -th iteration. The damping rate  $\alpha$  can be regarded as the step size of this iterative update. For a sampling rate of 10%, we select  $\alpha = 0.5$  to slow down the iterative update. However, for relatively higher sampling rates ( $\geq 15\%$ ), we can omit the damping step and choose  $\alpha = 1$ .

The L1 approach requires parameter tuning on a training dataset acquired under the same setting as the test data. The LSQ approach, on the other hand, does not require parameter tuning. The AMP-PE approach automatically and adaptively computes the MAP estimations of distribution parameters  $\theta, \tau_w$ . This characteristic makes it a convenient choice for clinical settings across various acquisition protocols and scanners. Unlike the LSQ and L1 approaches, which separate the recovery of VFA multi-echo images from the recovery of tissue parameters, the AMP-PE approach jointly recovers them by combining the VFA multi-echo image prior with the signal prior. Additionally, the maximum numbers of iterations for all three approaches are set to 100.

### 3.2 Comparison with the Gradient Support Pursuit Algorithm

We then proceed to compare AMP-PE with the model-based Gradient Support Pursuit (GraSP) algorithm [26]. GraSP, like AMP-PE, also performs a joint recovery of MR tissue parameters, it solves the following constrained maximum likelihood (ML) estimation:

$$\begin{aligned} \min_{z_0, t_1, t_2^*} \quad & \sum_{ij} \|\mathbf{y}_{ij} - \mathbf{A}_{ij}(\mathbf{f}_{ij}(z_0, t_1, t_2^*) \circ \exp(-\mathbf{i}\phi_{ij}))\|_2^2 \\ \text{subject to} \quad & \|\mathbf{H}z_0\|_0 \leq K_{z_0}, \quad \|\mathbf{H}t_1\|_0 \leq K_{t_1} \quad \text{and} \quad \|\mathbf{H}t_2^*\|_0 \leq K_{t_2^*}, \end{aligned} \quad (27)$$

where  $\phi_{ij}$  represents the phase image, “ $\circ$ ” denotes the component-wise product, the bold  $\mathbf{i}$  symbolizes the imaginary unit, and  $K_{z_0}, K_{t_1}, K_{t_2^*}$  denote the sparsity levels of the proton density,  $T_1$ , and  $T_2^*$  maps, respectively. The sparsity levels were tuned on the training set “R0” and were set to  $0.2N$ ,  $0.3N$ , and  $0.3N$ , respectively, to achieve optimal performance. As recommended in [26], the quantitative maps were rescaled to a common range to enhance accuracy and convergence speed. When it comes to the optimization of the quantitative maps  $z_0, t_1$  and  $t_2^*$ , GraSP’s objective function is formulated as the squared error in relation to the measurements  $\mathbf{y}_{ij}$  in the k-space, whereas the objective functions of LSQ, L1, and AMP-PE are formulated as the squared errors concerning the multi-echo images  $f_{ij}$  in the image domain in Section 3.1. Due to the non-convex nature of all these problems and the difference in the formulation of cost functions, the ground-truth reference image reconstructed from the fully-sampled data for GraSP differs from that of the other approaches. As such, the reconstruction errors of both GraSP and AMP-PE need to be computed relative to their respective reference images. However, the lack of a common reference makes it

unfeasible to compare reconstruction errors directly. Thus, the comparison between AMP-PE and GraSP primarily focuses on algorithmic stability, the need for parameter tuning, and computational efficiency.

## 4 Results

### 4.1 Comparison with the Least Squares and $l_1$ -norm Regularization Approaches

We first compare different approaches and undersampling schemes using the variable-density pattern. We subsequently highlight the performance differences between the variable-density and Poisson-disk patterns.

#### 4.1.1 Retrospective Undersampling with the Variable-density Pattern

Using a brain mask, we computed the normalized root mean square error (NRMSE) within the brain region. Specifically, the reciprocal of the  $T_2^*$  map, referred to as the  $R_2^*$  map, is frequently employed in brain studies [65,66]. Therefore, we computed the NRMSE with respect to the  $R_2^*$  map in this paper. Table 1 presents the NRMSEs of the recovered  $T_1$ ,  $R_2^*$ , and proton density maps for subject R1. Due to space constraints, the results for the remaining subjects, R2 to R5, are provided in Tables S1 to S4 in the Supporting Information. Across various sampling rates, both the L1 and AMP-PE approaches generally outperformed the LSQ approach. When the sampling rates were relatively lower at 10% and 15%, AMP-PE exhibited superior performance over L1, owing to its joint reconstruction of the tissue parameters. At a relatively higher sampling rate of 20%, both AMP-PE and L1 yielded comparable results. The L1 approach requires manual parameter tuning, whereas AMP-PE is equipped with built-in parameter estimation.

Different sampling schemes had varying effects on the recovered tissue parameters. Particularly, at low sampling rates of 10% and 15%, the performance differences among the schemes became more evident. Regarding  $T_1$  mapping, schemes U3 and U4 exhibited comparable performance, surpassing the performance of schemes U1 and U2. Concerning  $R_2^*$  mapping, schemes U1 and U2 showed similar performance, significantly outperforming schemes U3 and U4. In the case of proton density mapping, schemes U1 and U2 performed similarly well, outshining schemes U3 and U4.

As an example, we present the recovered images and the corresponding absolute errors for one slice of the 3D brain image from subject R1 at a sampling rate of 10%. They are shown in Fig. 3–Fig. 5. Due to space constraints, the recovered images at sampling rates of 15% and 20% are provided in Fig. S2–S7 in the Supporting Information. Visual inspection of the images aligns with the quantitative NRMSE findings.

The reconstruction experiments were conducted on the MATLAB platform using a machine (Intel Xeon Gold 5218 Processor, 2.30GHz) with 200 Gb RAM. Using the 15% case as an example, we compared the runtime of each method. The LSQ, L1 and AMP-PE approaches took 1.09, 4.23 and 5.67 hours respectively to complete the reconstruction process.



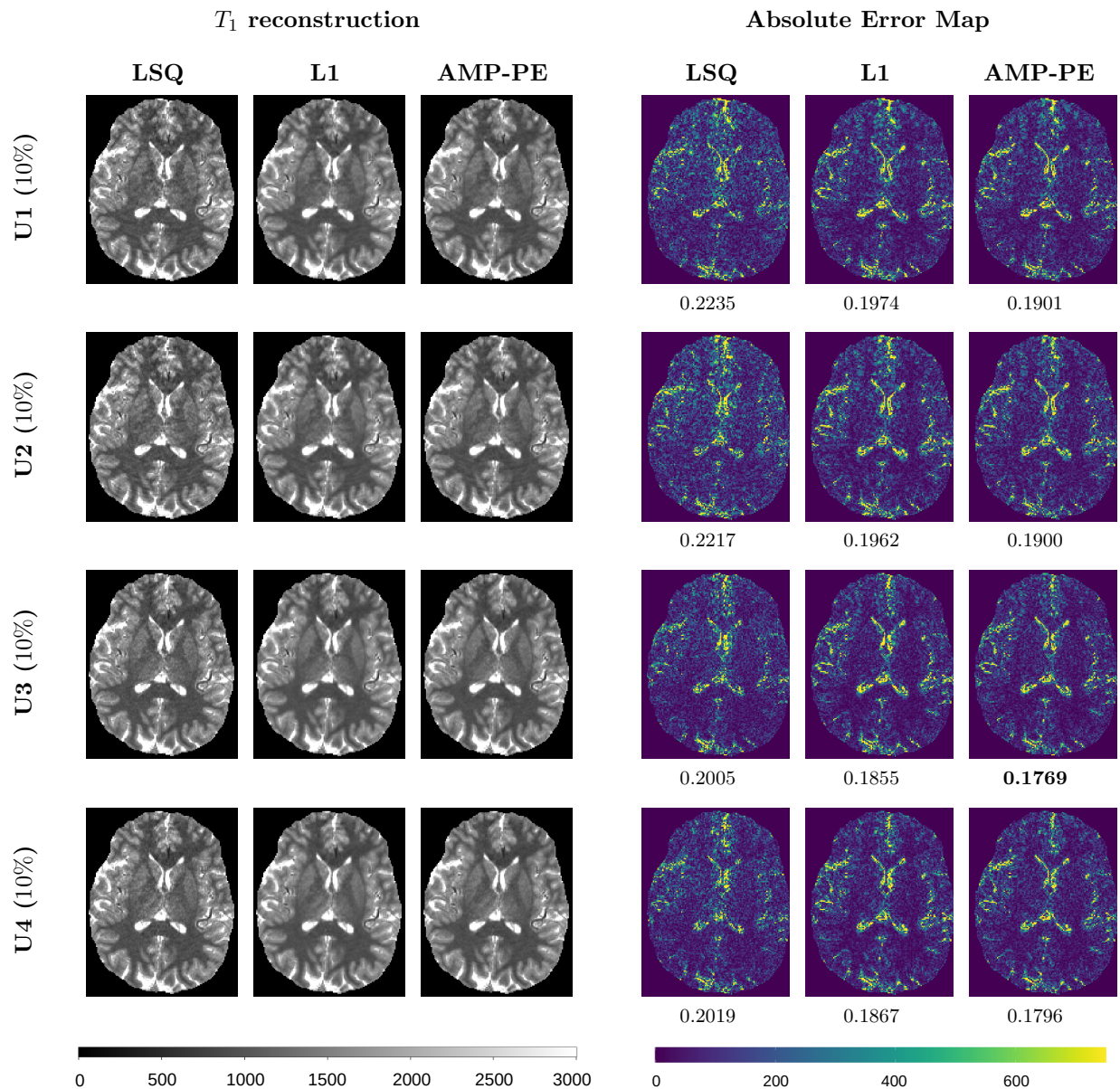


Figure 3: Retrospective undersampling with the variable-density pattern at the 10% undersampling rate: recovered  $T_1$  maps and absolute error maps from the subject R1 using three reconstruction approaches (LSQ, L1, AMP-PE) and four undersampling schemes (U1–U4). AMP-PE with the U3 scheme achieved the lowest NRMSE of 0.1769.

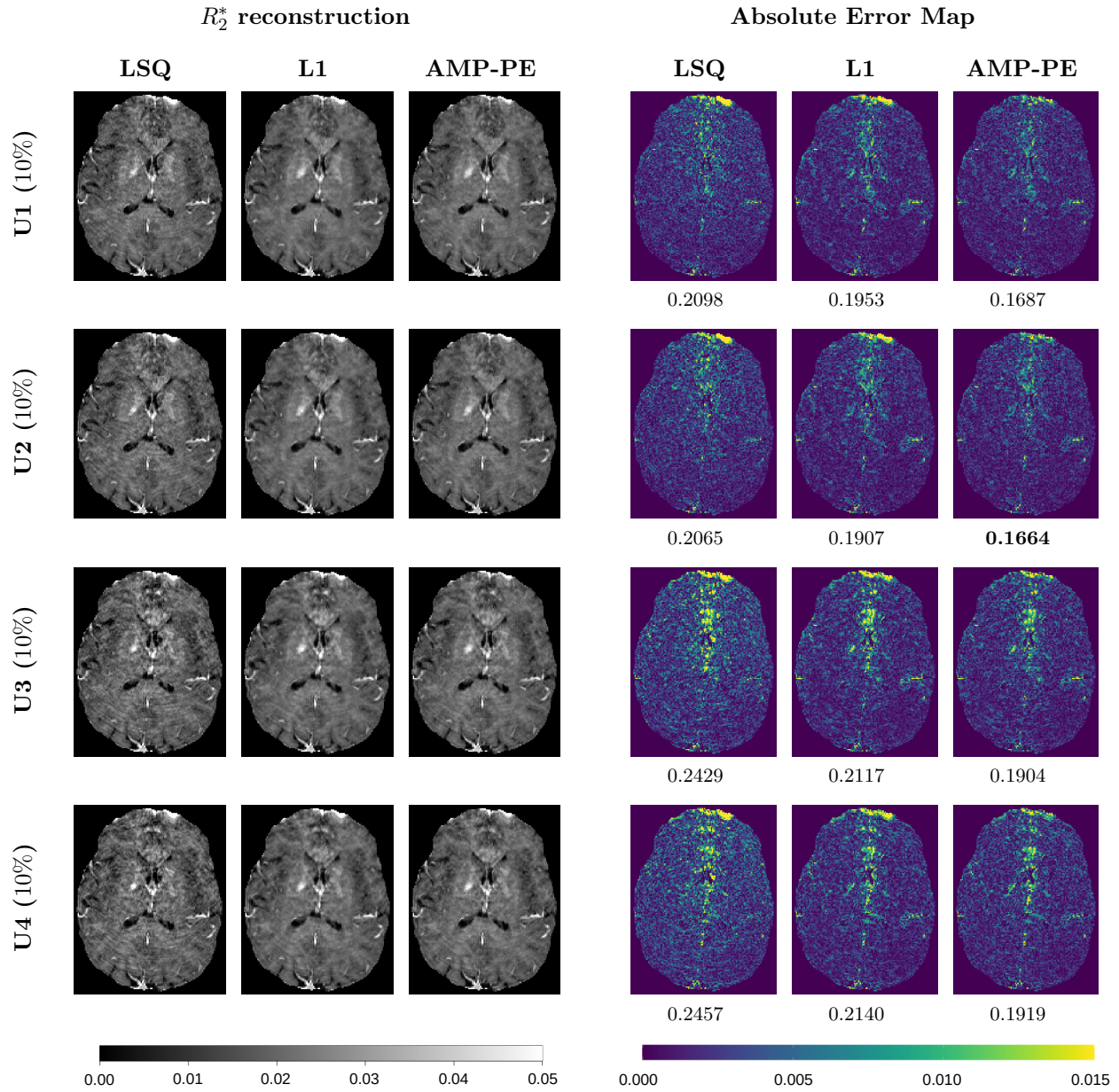


Figure 4: Retrospective undersampling with the variable-density pattern at the 10% undersampling rate: recovered  $R_2^*$  maps and absolute error maps from the subject R1 using three reconstruction approaches (LSQ, L1, AMP-PE) and four undersampling schemes (U1–U4). AMP-PE with the U2 scheme achieved the lowest NRMSE of 0.1664.



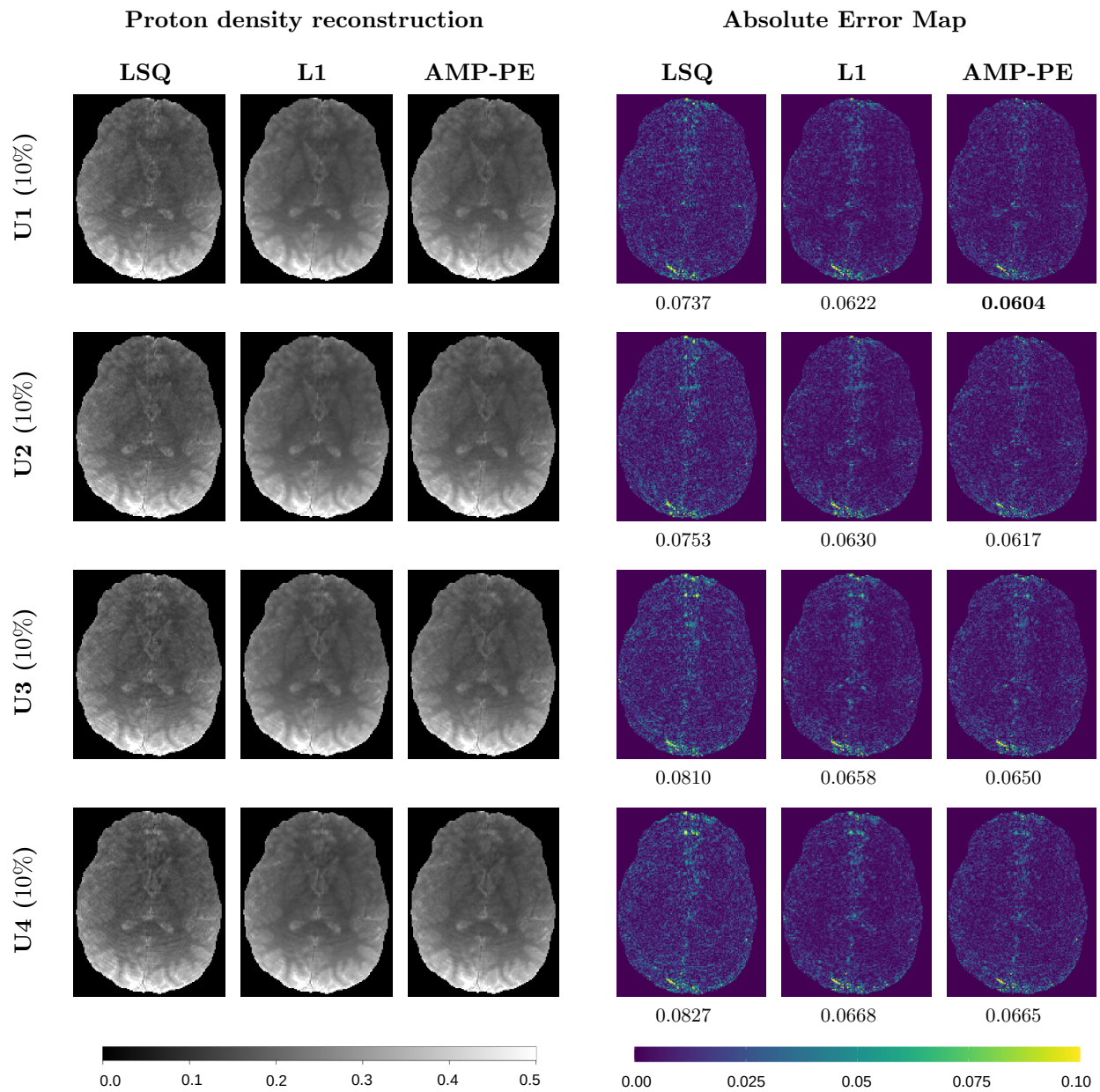


Figure 5: Retrospective undersampling with the variable-density pattern at the 10% undersampling rate: recovered proton density maps and absolute error maps from the subject R1 using three reconstruction approaches (LSQ, L1, AMP-PE) and four undersampling schemes (U1–U4). AMP-PE with the U1 scheme achieved the lowest NRMSE of 0.0604.

Table 1: Retrospective undersampling with the variable-density pattern: normalized root mean square errors of recovered  $T_1$ ,  $R_2^*$  and proton density  $Z_0$  maps from the subject R1 at different sampling rates (10%, 15%, 20%). Three reconstruction approaches (LSQ, L1, AMP-PE) with four undersampling schemes (U1–U4) are compared in this table.

		10%			15%			20%		
		LSQ	L1	AMP-PE	LSQ	L1	AMP-PE	LSQ	L1	AMP-PE
$\hat{t}_1$	U1	0.2235	0.1974	0.1901	0.1784	0.1545	0.1530	0.1560	0.1358	0.1362
	U2	0.2217	0.1962	0.1900	0.1764	0.1542	0.1520	0.1574	0.1370	0.1383
	U3	0.2005	0.1855	<b>0.1769</b>	0.1667	0.1498	<b>0.1455</b>	0.1497	0.1324	<b>0.1323</b>
	U4	0.2019	0.1867	0.1796	0.1696	0.1496	0.1465	0.1507	0.1327	0.1324
$\hat{r}_2^*$	U1	0.2098	0.1953	0.1687	0.1355	0.1190	0.1159	0.1094	<b>0.0953</b>	0.0972
	U2	0.2065	0.1907	<b>0.1664</b>	0.1352	0.1191	<b>0.1157</b>	0.1106	0.0961	0.0984
	U3	0.2429	0.2117	0.1904	0.1584	0.1311	0.1315	0.1248	0.1031	0.1084
	U4	0.2457	0.2140	0.1919	0.1597	0.1324	0.1337	0.1253	0.1038	0.1093
$\hat{z}_0$	U1	0.0737	0.0622	<b>0.0604</b>	0.0538	<b>0.0438</b>	0.0462	0.0445	<b>0.0366</b>	0.0400
	U2	0.0753	0.0630	0.0617	0.0549	0.0445	0.0470	0.0451	0.0371	0.0407
	U3	0.0810	0.0658	0.0650	0.0586	0.0461	0.0498	0.0472	0.0379	0.0424
	U4	0.0827	0.0668	0.0665	0.0601	0.0472	0.0512	0.0481	0.0384	0.0430

#### 4.1.2 Prospective Undersampling with the Variable-density Pattern

The results obtained from retrospective undersampling revealed that schemes U1 and U2 exhibited similar performance in terms of  $R_2^*$  and proton density mapping, while schemes U3 and U4 demonstrated similar performance in  $T_1$  mapping. Additionally, U2 and U4 proved to be more straightforward to implement within the acquisition protocol as they did not require different sampling patterns across echo times. Hence, for prospective undersampling in the clinical setting, we opted for U2 and U4. It is important to note that in this scenario, we lacked access to ground-truth reference images needed for calculating NRMSE values. Taking one slice from the 3D brain image from the subject P1 for example, we showcase the recovered images using the L1 and AMP-PE approaches when the sampling rate was 10% in Fig. 6. The recovered images for sampling rates of 15% and 20% are provided in Fig. S8–S9 in the Supporting Information. A visual inspection indicates that the prospective undersampling scheme yields comparable and consistent results to the retrospective case.

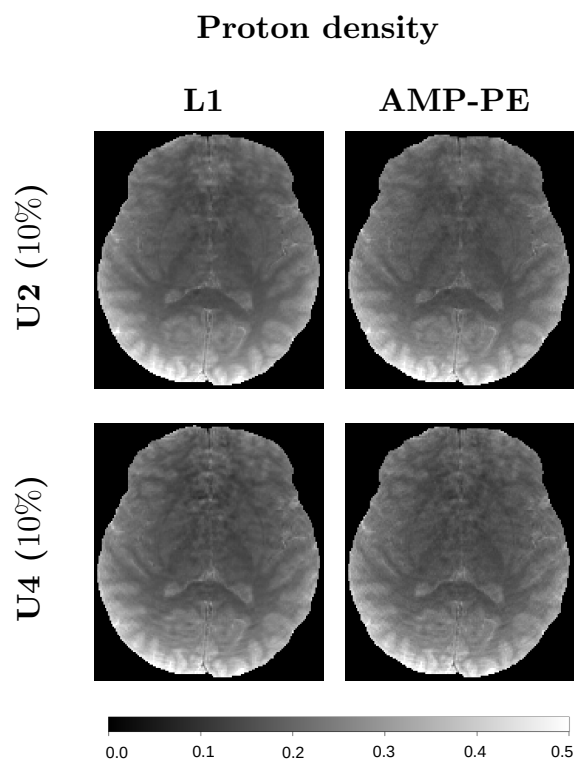
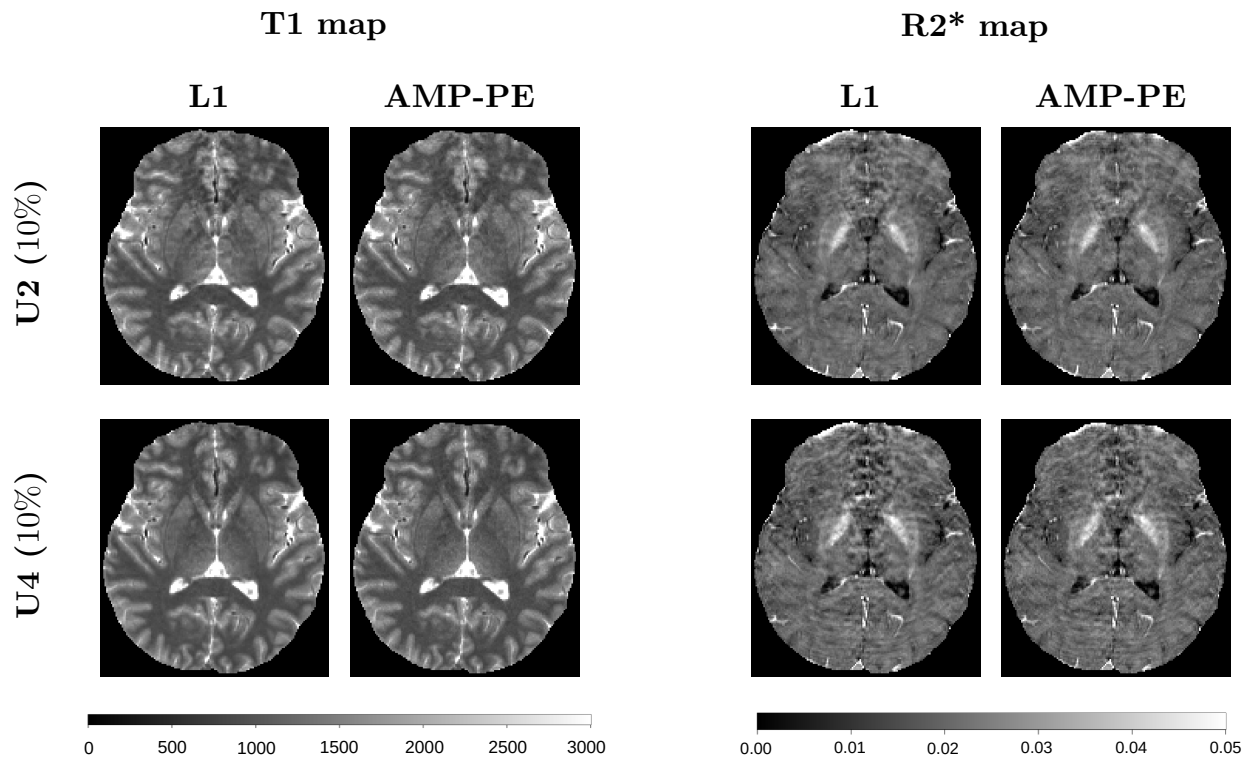


Figure 6: Prospective undersampling with the variable-density pattern at the 10% undersampling rate: recovered tissue parameters and absolute error maps from the subject P1 using two reconstruction approaches (L1, AMP-PE) and two undersampling schemes (U2, U4).

Table 2: Retrospective undersampling: normalized root mean square errors of recovered  $T_1$ ,  $R_2^*$  and proton density  $Z_0$  maps from the subject R1 at different sampling rates (10%, 15%, 20%). Using AMP-PE as the reconstruction approach, the variable-density (VD) and Poisson-disk (PD) patterns with selected sampling schemes (U2, U4) are compared in this table.

		10%		15%		20%	
		VD	PD	VD	PD	VD	PD
$\hat{t}_1$	U4	<b>0.1796</b>	0.1939	0.1465	<b>0.1427</b>	0.1324	<b>0.1270</b>
$\hat{r}_2^*$	U2	<b>0.1664</b>	0.2154	0.1157	<b>0.1133</b>	0.0984	<b>0.0900</b>
$\hat{z}_0$	U2	<b>0.0617</b>	0.0764	0.0470	<b>0.0448</b>	0.0407	<b>0.0362</b>

### 4.1.3 Comparison of Variable-density and Poisson-disk Sampling Patterns

By utilizing the AMP-PE reconstruction approach with U2 and U4 as the undersampling schemes, we can emphasize the performance distinctions between variable-density (VD) and Poisson-disk (PD) patterns, as showcased in Table 2. Comprehensive results pertaining to PD, including other approaches and sampling schemes, can be found in Tables S5-S10 of the Supporting Information. Notably, when the sampling rate was 10%, VD exhibited significantly superior performance compared to PD. Conversely, at sampling rates of 15% and 20%, PD outperformed VD. For instance, considering a selected slice from the 3D brain image of subject P1, the recovered  $T_1$ ,  $R_2^*$  and proton density maps are shown in Fig. S10-S12 of the Supporting Information. Visual inspection confirms that VD indeed outperforms PD in the case of 10% sampling rate. However, for the 15% and 20% cases, the superiority of one pattern over the other may vary depending on different brain regions, with PD achieving an overall lower NRMSE.

## 4.2 Comparison with the Gradient Support Pursuit Algorithm

We compared GraSP and AMP-PE using the U1 retrospective undersampling scheme with the VD pattern. Taking one slice from the subject R1 for example, we showcase the recovered  $T1$  maps and absolute error maps across different sampling rates in Fig. 7. The recovered  $R_2^*$  and proton density maps are shown in Fig. S13-S14, and the NRMSEs of recovered images are provided in Table S10 of the Supporting Information. The results showed that GraSP produced more errors compared to AMP-PE. GraSP employs a second-order quasi-Newton method to minimize the objective function [67]. However, the use of second-order methods can often result in entrapment within local optima during optimization. Consequently, the images reconstructed by GraSP, with 100 iterations, exhibited more errors in contrast to those with 10 iterations. On the other hand, AMP-PE optimizes the tissue parameters in an alternating fashion. The problem presented in (21) is effectively broken down into three separate one-dimensional problems concerning  $z_0$ ,  $t_1$ , and  $t_2^*$ . This approach allows each 1D problem’s global optimum to be determined exactly, either through a convex solution or exhaustive search. While the solution achieved using this method is still not guaranteed to be the global optimum of (21), the results shown in Fig. 7 suggest that AMP-PE’s methodology proves to be more robust than GraSP’s second-order approach. Finally, taking the reconstruction of a 2D slice in the 15% case for example, GraSP (with 10 iterations) and AMP-PE (with 100 iterations) took 4.1 and 4.9 minutes respectively to complete.

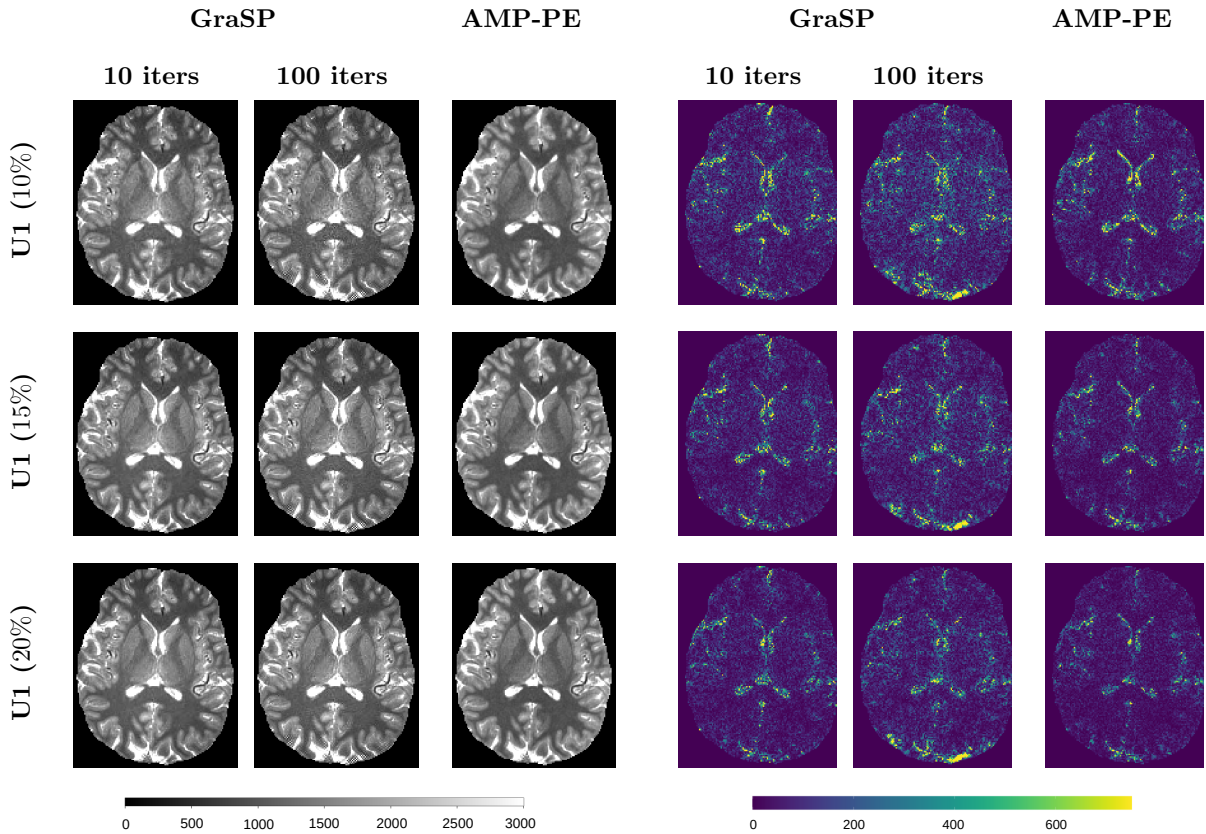


Figure 7: Retrospective undersampling with the variable-density pattern: recovered  $T_1$  maps and absolute error maps from the subject R1 using GraSP and AMP-PE approaches and U1 undersampling schemes. The recovered images by GraSP with 100 iterations have more errors than those with 10 iterations.



## 5 Discussion

Equipped with automatic and adaptive hyperparameter estimation, the proposed nonlinear AMP-PE framework integrates the VFA multi-echo image prior and the signal model prior to jointly recover MR tissue parameters. Notably, we observe that the benefits of joint reconstruction are more pronounced at lower sampling rates, specifically 10% and 15%. At the 20% sampling rate, where more data are available, the VFA multi-echo image prior assumes a dominant role, surpassing the significance of the signal model prior. The signal model prior is enforced on the signal magnitudes of each voxel across different flip angles and echo times, representing a voxel-wise local prior. Conversely, the VFA multi-echo image prior originates from the sparse prior on image wavelet coefficients. As the wavelet transform  $\mathbf{H}$  is applied to the entire image, the sparse prior, and therefore the VFA multi-echo image prior, can be considered as global priors in this context.

The convergence of AMP has only been established for linear random Gaussian measurement systems [13]. Establishing convergence guarantees for general measurement systems remains an open question. When the sampling rate was as low as 10%, we employed the damping operation on the wavelet coefficients  $\mathbf{v}$  in equation (26) to ensure the stability of the nonlinear AMP-PE convergence. Additionally, by leveraging a dictionary-based exhaustive search, the nonlinear AMP-PE solves a nonconvex problem to reconstruct tissue parameters in an alternating fashion. It is worth noting that the initialization step plays a crucial role in achieving convergence and avoiding getting stuck in unfavorable local optima. In our study, we discovered that the least-squares solution served as a suitable initialization for AMP-PE.

AMP-PE treats the distribution parameters  $\lambda, \tau_w$  as variables and is capable of computing their posterior distributions  $p(\lambda|\mathbf{y})$  and  $p(\tau_w|\mathbf{y})$  through message passing. However, unlike the posterior distributions of the actual “image” variables  $x, z, v$ , the distributions  $p(\lambda|\mathbf{y})$  and  $p(\tau_w|\mathbf{y})$  are not approximated as Gaussians in AMP-PE. Therefore, accurately computing the MAP estimations of these parameters becomes challenging since closed-form solutions are typically unavailable. To address this, we relied on a second-order method to compute the MAP estimations of these parameters. To ensure a favorable starting point and avoid undesirable local optima, we initialized the distribution parameters using maximum likelihood estimations based on the least-squares solutions. Additionally, the damping operation can also be applied to the estimated parameters if necessary<sup>1</sup>.

Experiments have revealed that both the sampling scheme and sampling pattern in a 3D GRE sequence have an impact on the reconstructed tissue parameters. There is no one-size-fits-all sampling scheme that is suitable for all types of reconstructions. Schemes U1 and U2 are better suited for  $T_2^*$  and proton density mapping, while U3 and U4 are more appropriate for  $T_1$  mapping. In practical applications, we recommend adopting schemes U2 and U4 for easier implementation in prospective undersampling. As depicted in Fig. 2, the variable-density (VD) pattern acquires a greater number of low-frequency samples, whereas the Poisson-disk (PD) pattern acquires more

---

<sup>1</sup>In this study, we did not apply damping to the distribution parameters as the damping applied to the wavelet coefficients had already stabilized AMP-PE for the 10% sampling rate case.

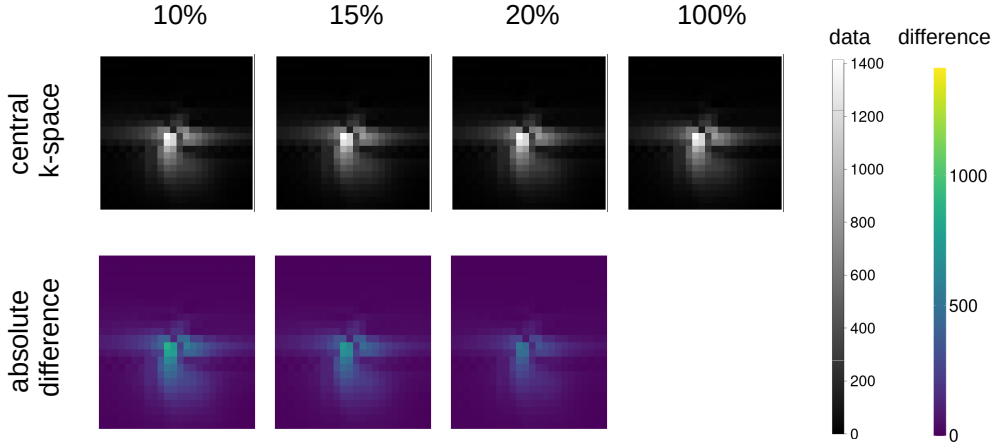


Figure 8: Prospective undersampling: the  $24 \times 24$  central k-space data acquired at different sampling rates (10%, 15%, 20%, 100%). The absolute differences between the undersampled and fully-sampled cases depend on the signal magnitude as well as the sampling rate.

high-frequency samples due to its uniform sampling in  $k$ -space. When the sampling rate is relatively low at 10%, the results in Table 2 demonstrate that having more low-frequency measurements leads to better performance. However, as the sampling rates increase to 15% and 20%, high-frequency measurements become more influential, contributing significantly to image quality by capturing more detailed structural information.

In prospective undersampling, we do not have access to ground-truth reference images. Fig. 8 illustrates a comparison of the central k-space data acquired at different sampling rates. The absolute differences in k-space data between the undersampled and fully-sampled cases depend on both the signal magnitude and the sampling rate. Larger signal magnitudes within each undersampled case correspond to larger absolute differences. As the undersampling rate increases, the absolute difference decreases. Consequently, reconstructions based on fully-sampled data cannot serve as reliable ground-truth references in prospective undersampling scenarios, and quantitative evaluations can only be conducted in retrospective undersampling cases.

## 6 Conclusion

We proposed a Bayesian formulation that combines the signal model and sparse prior on VFA multi-echo images to achieve a model-based joint recovery of  $T_1$ ,  $T_2^*$ , and proton density maps. We designed nonlinear AMP-PE for probabilistic inferences and the reconstruction of quantitative maps. The proposed AMP-PE framework offers automatic and adaptive hyperparameter estimation capabilities, making it a convenient choice for clinical settings with varying acquisition protocols and scanners. The model-based joint recovery approach outperformed the decoupled methods in *in vivo* experiments. Additionally, we explored the use of complementary undersampling patterns in quantitative MRI to further enhance image quality. Our experiments revealed that identical sampling patterns across different echo times are suitable for  $T_1$  mapping, while complementary



patterns across different flip angles are beneficial for  $T_2^*$  and proton density mappings.

## A Message Passing Steps

### 1) Message passing from $\{z_{ijn}\}$ to $\mathcal{T}_n$ .

The message from  $\Gamma_{ijn}$  to  $x_{ijn}$  can be calculated as follows:

$$\begin{aligned}\Delta_{\Gamma_{ijn} \rightarrow x_{ijn}} &= \log \int \Gamma_{ijn}(x_{ijn}, z_{ijn}) \cdot \exp(\Delta_{z_{ijn} \rightarrow \Gamma_{ijn}}) dz_{ijn} \\ &\approx -\frac{1}{2\pi\tau_1(z_{ijn})} \left( x_{ijn} - \left| \mu_1(z_{ijn}) \right| \right)^2 + C.\end{aligned}\quad (28)$$

The message from  $x_{ijn}$  to  $\Psi_{ijn}$  is

$$\Delta_{x_{ijn} \rightarrow \Psi_{ijn}} = \Delta_{\Gamma_{ijn} \rightarrow x_{ijn}}. \quad (29)$$

The message from  $\Psi_{ijn}$  to the tissue parameters  $\mathcal{T}_n = \{z_0(n), t_1(n), t_2^*(n)\}$  is

$$\begin{aligned}\Delta_{\Psi_{ijn} \rightarrow \mathcal{T}_n} &= \log \int \Psi_{ijn}(x_{ijn}, z_0(n), t_1(n), t_2^*(n)) \cdot \exp(\Delta_{x_{ijn} \rightarrow \Psi_{ijn}}) dz_{ijn} \\ &= -\frac{1}{2\pi\tau_1(z_{ijn})} \left( f_{ij}(z_0(n), t_1(n), t_2^*(n)) - \left| \mu_1(z_{ijn}) \right| \right)^2.\end{aligned}\quad (30)$$

### 2) Message passing from $\mathcal{T}_n$ to $\{z_{ijn}\}$ .

We can perform the message passing from  $\mathcal{T}_n$  to  $\{z_{ijn}\}$  in a similar fashion. Specifically, the message from  $\Psi_{ijn}$  to  $x_{ijn}$  is

$$\begin{aligned}\Delta_{\Psi_{ijn} \rightarrow x_{ijn}} &= \log \Psi(x_{ijn}, z_0(n), t_1(n), t_2^*(n)) \\ &= \log \delta(x_{ijn} - f_{ij}(z_0(n), t_1(n), t_2^*(n))).\end{aligned}\quad (31)$$

The message from  $x_{ijn}$  to  $\Gamma_{ijn}$  is

$$\Delta_{x_{ijn} \rightarrow \Gamma_{ijn}} = \Delta_{\Psi_{ijn} \rightarrow x_{ijn}}. \quad (32)$$

The message from  $\Gamma_{ijn}$  to  $z_{ijn}$  is

$$\begin{aligned}\Delta_{\Gamma_{ijn} \rightarrow z_{ijn}} &= \log \int \Gamma_{ijn}(x_{ijn}, z_{ijn}) \cdot \exp(\Delta_{x_{ijn} \rightarrow \Gamma_{ijn}}) dx_{ijn} \\ &= \log \delta(|z_{ijn}| - f_{ij}(z_0(n), t_1(n), t_2^*(n))).\end{aligned}\quad (33)$$

Combining the messages from  $\Gamma_{ijn}$ ,  $\{\Phi_{ijm}\}$  and the VFA multi-echo image prior  $\Xi_{ijn}$ , we can

finally calculate the posterior distribution of  $z_{ijn}$  as follows:

$$\begin{aligned}
p(z_{ijn}|\mathbf{y}) &\propto \exp\left(\Delta_{\Gamma_{ijn} \rightarrow z_{ijn}} + \log \Xi_{ijn}(z_{ijn}) + \sum_m \Delta_{\Phi_{ijm} \rightarrow z_{ijn}}\right) \\
&\propto \exp\left(-\frac{1}{\pi\tau_2(z_{ijn})} \left|z_{ijn} - \mu_2(z_{ijn})\right|^2\right) \cdot \exp\left(\sum_m \Delta_{\Phi_{ijm} \rightarrow z_{ijn}}\right),
\end{aligned} \tag{34}$$

where  $\mu_2(z_{ijn})$ ,  $\tau_2(z_{ijn})$  are the corresponding mean and variance:

$$\mu_2(z_{ijn}) = f_{ij}(z_0(n), t_1(n), t_2^*(n)) \cdot \frac{\mu_s(z_{ijn})}{|\mu_s(z_{ijn})|} \tag{35}$$

$$\tau_2(z_{ijn}) = \tau_s(z_{ijn}) \cdot \tag{36}$$

The above  $\mu_s(z_{ijn})$ ,  $\tau_s(z_{ijn})$  are the mean and variance of the VFA multi-echo image prior  $\Xi_{ijn}(z_{ijn})$  in (14),(16).

The posterior  $p(z_{ijn}|\mathbf{y})$  in (34) can be further simplified as

$$p(z_{ijn}|\mathbf{y}) \propto \exp\left(-\frac{1}{\pi\tau(z_{ijn})} \left|z_{ijn} - \mu(z_{ijn})\right|^2\right), \tag{37}$$

where  $\mu(z_{ijn})$ ,  $\tau(z_{ijn})$  are the corresponding mean and variance.

## References

- [1] S. Eminian, S. D. Hajdu, R. A. Meuli, P. Maeder, and P. Hagmann, “Rapid high resolution t1 mapping as a marker of brain development: Normative ranges in key regions of interest,” *PLoS One*, vol. 13, no. 6, pp. 1932–6203, 2018.
- [2] S. Lee, R.-E. Yoo, S. H. Choi, S.-H. Oh, S. Ji, J. Lee, K. Y. Huh, J. Y. Lee, I. Hwang, K. M. Kang, T. J. Yun, J.-h. Kim, and C.-H. Sohn, “Contrast-enhanced mri t1 mapping for quantitative evaluation of putative dynamic glymphatic activity in the human brain in sleep-wake states,” *Radiology*, vol. 300, no. 3, pp. 661–668, 2021.
- [3] M. Ulla, J. M. Bonny, L. Ouchchane, I. Rieu, B. Claise, and F. Durif, “Is r2\* a new mri biomarker for the progression of parkinson’s disease? a longitudinal follow-up,” *PLOS ONE*, vol. 8, pp. 1–8, 03 2013.
- [4] J. Acosta-Cabronero, M. J. Betts, A. Cardenas-Blanco, S. Yang, and P. J. Nestor, “In vivo mri mapping of brain iron deposition across the adult lifespan,” *Journal of Neuroscience*, vol. 36, no. 2, pp. 364–374, 2016.
- [5] Q. Lin, S. Shahid, A. Hone-Blanchet, S. Huang, J. Wu, A. Bisht, D. Loring, F. Goldstein, A. Levey, B. Crosson, J. Lah, and D. Qiu, “Magnetic resonance evidence of increased iron con-

- tent in subcortical brain regions in asymptomatic alzheimer’s disease,” *Human Brain Mapping*, vol. 44, no. 8, pp. 3072–3083, 2023.
- [6] S. Taheri, C. Gasparovic, N. J. Shah, and G. A. Rosenberg, “Quantitative measurement of blood-brain barrier permeability in human using dynamic contrast-enhanced mri with fast t1 mapping,” *Magnetic Resonance in Medicine*, vol. 65, no. 4, pp. 1036–1042, 2011.
- [7] E. J. Candès, J. Romberg, and T. Tao, “Robust uncertainty principles: Exact signal reconstruction from highly incomplete frequency information,” *IEEE Trans. Inf. Theory*, vol. 52(2), pp. 489–509, 2006.
- [8] D. L. Donoho, “Compressed sensing,” *IEEE Trans. Inf. Theory*, vol. 52, no. 4, pp. 1289–1306, 2006.
- [9] I. Daubechies, *Ten lectures on wavelets*. Philadelphia, PA, USA: Society for Industrial and Applied Mathematics, 1992.
- [10] E. J. Candès, J. K. Romberg, and T. Tao, “Stable signal recovery from incomplete and inaccurate measurements,” *Communications on Pure and Applied Mathematics*, vol. 59, no. 8, pp. 1207–1223, 2006.
- [11] A. Y. Yang, A. Ganesh, Z. Zhou, S. S. Sastry, and Y. Ma, “A review of fast l1-minimization algorithms for robust face recognition,” *CoRR*, vol. abs/1007.3753, 2010.
- [12] D. Baron, S. Sarvotham, and R. G. Baraniuk, “Bayesian compressive sensing via belief propagation,” *IEEE Trans. Signal Process.*, vol. 58, no. 1, pp. 269–280, 2010.
- [13] S. Rangan, “Generalized approximate message passing for estimation with random linear mixing,” in *Proceedings of IEEE ISIT*, pp. 2168–2172, July 2011.
- [14] S. Huang and T. D. Tran, “Sparse signal recovery using generalized approximate message passing with built-in parameter estimation,” in *Proceedings of IEEE ICASSP*, pp. 4321–4325, March 2017.
- [15] S. Huang and T. D. Tran, “Sparse signal recovery via generalized entropy functions minimization,” *IEEE Transactions on Signal Processing*, vol. 67, no. 5, pp. 1322–1337, 2019.
- [16] J. P. Haldar and Z.-P. Liang, “Joint reconstruction of noisy high-resolution mr image sequences,” in *2008 5th IEEE International Symposium on Biomedical Imaging: From Nano to Macro*, pp. 752–755, 2008.
- [17] B. Zhao, W. Lu, T. K. Hitchens, F. Lam, C. Ho, and Z.-P. Liang, “Accelerated mr parameter mapping with low-rank and sparsity constraints,” *Magnetic Resonance in Medicine*, vol. 74, no. 2, pp. 489–498, 2015.
- [18] J. Trzasko and A. Manduca, “Group sparse reconstruction of vector-valued images,” in *Proceedings of ISMRM*, 2011.

- [19] B. Bilgic, T. H. Kim, C. Liao, M. K. Manhard, L. L. Wald, J. P. Haldar, and K. Setsompop, “Improving parallel imaging by jointly reconstructing multi-contrast data,” *Magnetic Resonance in Medicine*, vol. 80, no. 2, pp. 619–632, 2018.
- [20] A. G. Christodoulou, J. L. Shaw, C. Nguyen, Q. Yang, Y. Xie, N. Wang, and D. Li, “Magnetic resonance multitasking for motion-resolved quantitative cardiovascular imaging,” *Nature Biomedical Engineering*, vol. 2, no. 2, pp. 215–226, 2018.
- [21] J. I. Tamir, M. Uecker, W. Chen, P. Lai, M. T. Alley, S. S. Vasanawala, and M. Lustig, “T2 shuffling: Sharp, multicontrast, volumetric fast spin-echo imaging,” *Magnetic Resonance in Medicine*, vol. 77, no. 1, pp. 180–195, 2017.
- [22] A. Bustin, G. Lima da Cruz, O. Jaubert, K. Lopez, R. M. Botnar, and C. Prieto, “High-dimensionality undersampled patch-based reconstruction (hd-prost) for accelerated multi-contrast mri,” *Magnetic Resonance in Medicine*, vol. 81, no. 6, pp. 3705–3719, 2019.
- [23] J. P. Haldar, D. Hernando, and Z.-P. Liang, “Super-resolution reconstruction of mr image sequences with contrast modeling,” in *2009 IEEE International Symposium on Biomedical Imaging: From Nano to Macro*, pp. 266–269, 2009.
- [24] K. T. Block, M. Uecker, and J. Frahm, “Model-based iterative reconstruction for radial fast spin-echo mri,” *IEEE Transactions on Medical Imaging*, vol. 28, no. 11, pp. 1759–1769, 2009.
- [25] T. J. Sumpf, M. Uecker, S. Boretius, and J. Frahm, “Model-based nonlinear inverse reconstruction for t2 mapping using highly undersampled spin-echo mri,” *Journal of Magnetic Resonance Imaging*, vol. 34, no. 2, pp. 420–428, 2011.
- [26] B. Zhao, F. Lam, and Z.-P. Liang, “Model-based mr parameter mapping with sparsity constraints: Parameter estimation and performance bounds,” *IEEE Transactions on Medical Imaging*, vol. 33, no. 9, pp. 1832–1844, 2014.
- [27] B. Zhao, K. Setsompop, H. Ye, S. F. Cauley, and L. L. Wald, “Maximum likelihood reconstruction for magnetic resonance fingerprinting,” *IEEE Transactions on Medical Imaging*, vol. 35, no. 8, pp. 1812–1823, 2016.
- [28] M. Akçakaya, S. Weingärtner, T. A. Basha, S. Roujol, S. Bellm, and R. Nezafat, “Joint myocardial t1 and t2 mapping using a combination of saturation recovery and t2-preparation,” *Magnetic Resonance in Medicine*, vol. 76, no. 3, pp. 888–896, 2016.
- [29] Y. Zhu, X. Peng, Y. Wu, E. X. Wu, L. Ying, X. Liu, H. Zheng, and D. Liang, “Direct diffusion tensor estimation using a model-based method with spatial and parametric constraints,” *Medical Physics*, vol. 44, no. 2, pp. 570–580, 2017.
- [30] Y. Guo, S. G. Lingala, Y. Zhu, R. M. Lebel, and K. S. Nayak, “Direct estimation of tracer-kinetic parameter maps from highly undersampled brain dynamic contrast enhanced mri,” *Magnetic Resonance in Medicine*, vol. 78, no. 4, pp. 1566–1578, 2017.

- [31] X. Wang, V. Roeloffs, J. Klosowski, Z. Tan, D. Voit, M. Uecker, and J. Frahm, “Model-based t1 mapping with sparsity constraints using single-shot inversion-recovery radial flash,” *Magnetic Resonance in Medicine*, vol. 79, no. 2, pp. 730–740, 2018.
- [32] X. Wang, F. Kohler, C. Unterberg-Buchwald, J. Lotz, J. Frahm, and M. Uecker, “Model-based myocardial t1 mapping with sparsity constraints using single-shot inversion-recovery radial flash cardiovascular magnetic resonance,” *Journal of Cardiovascular Magnetic Resonance*, vol. 21, no. 60, pp. 1–11, 2019.
- [33] X. Wang, Z. Tan, N. Scholand, V. Roeloffs, and M. Uecker, “Physics-based reconstruction methods for magnetic resonance imaging,” *Philosophical Transactions of the Royal Society A: Mathematical, Physical and Engineering Sciences*, vol. 379, no. 2200, p. 20200196, 2021.
- [34] W. Bano, G. F. Piredda, M. Davies, I. Marshall, M. Golbabaei, R. Meuli, T. Kober, J.-P. Thiran, and T. Hilbert, “Model-based super-resolution reconstruction of t2 maps,” *Magnetic Resonance in Medicine*, vol. 83, no. 3, pp. 906–919, 2020.
- [35] D. L. Donoho, A. Maleki, and A. Montanari, “Message-passing algorithms for compressed sensing,” *Proceedings of the National Academy of Sciences*, vol. 106, no. 45, pp. 18914–18919, 2009.
- [36] F. Krzakala, M. Mézard, F. Sausset, Y. F. Sun, and L. Zdeborová, “Statistical-physics-based reconstruction in compressed sensing,” *Phys. Rev. X*, vol. 2, p. 021005, May 2012.
- [37] F. Krzakala, M. Mézard, F. Sausset, Y. Sun, and L. Zdeborová, “Probabilistic reconstruction in compressed sensing: algorithms, phase diagrams, and threshold achieving matrices,” *J. Stat. Mech. Theory Exp.*, vol. 2012, p. P08009, aug 2012.
- [38] J. P. Vila and P. Schniter, “Expectation-maximization gaussian-mixture approximate message passing,” *IEEE Transactions on Signal Processing*, vol. 61, no. 19, pp. 4658–4672, 2013.
- [39] S. Huang, D. Qiu, and T. D. Tran, “Approximate message passing with parameter estimation for heavily quantized measurements,” *IEEE Transactions on Signal Processing*, vol. 70, pp. 2062–2077, 2022.
- [40] S. Huang, J. J. Lah, J. W. Allen, and D. Qiu, “Robust quantitative susceptibility mapping via approximate message passing with parameter estimation,” *Magnetic Resonance in Medicine*, vol. 90, no. 4, pp. 1414–1430, 2023.
- [41] J. Ziniel and P. Schniter, “Dynamic compressive sensing of time-varying signals via approximate message passing,” *IEEE Transactions on Signal Processing*, vol. 61, no. 21, pp. 5270–5284, 2013.
- [42] C. Millard, A. T. Hess, B. Mailhe, and J. Tanner, “An approximate message passing algorithm for rapid parameter-free compressed sensing mri,” in *2020 IEEE International Conference on Image Processing (ICIP)*, pp. 91–95, 2020.

- [43] X. Qiao, J. Du, L. Wang, Z. He, and Y. Jia, “A model-based deep network for mri reconstruction using approximate message passing algorithm,” in *2020 IEEE International Conference on Acoustics, Speech and Signal Processing (ICASSP)*, pp. 1105–1109, 2020.
- [44] A. Rich, L. C. Potter, N. Jin, J. Ash, O. P. Simonetti, and R. Ahmad, “A bayesian model for highly accelerated phase-contrast mri,” *Magnetic Resonance in Medicine*, vol. 76, no. 2, pp. 689–701, 2016.
- [45] A. Rich, L. C. Potter, N. Jin, Y. Liu, O. P. Simonetti, and R. Ahmad, “A bayesian approach for 4d flow imaging of aortic valve in a single breath-hold,” *Magnetic Resonance in Medicine*, vol. 81, no. 2, pp. 811–824, 2019.
- [46] A. Pruitt, A. Rich, Y. Liu, N. Jin, L. Potter, M. Tong, S. Rajpal, O. Simonetti, and R. Ahmad, “Fully self-gated whole-heart 4d flow imaging from a 5-minute scan,” *Magnetic Resonance in Medicine*, vol. 85, no. 3, pp. 1222–1236, 2020.
- [47] S. Huang, J. J. Lah, J. W. Allen, and D. Qiu, “A probabilistic bayesian approach to recover  $r2^*$  map and phase images for quantitative susceptibility mapping,” *Magnetic Resonance in Medicine*, vol. 88, no. 4, pp. 1624–1642, 2022.
- [48] J. Y. Cheng, T. Zhang, M. T. Alley, M. Lustig, S. S. Vasanawala, and J. M. Pauly, “Variable-density radial view-ordering and sampling for time-optimized 3d cartesian imaging,” in *Proceedings of the ISMRM Workshop on Data Sampling and Image Reconstruction*, April 2013.
- [49] S. Vasanawala, M. Murphy, M. Alley, P. Lai, K. Keutzer, J. Pauly, and M. Lustig, “Practical parallel imaging compressed sensing mri: Summary of two years of experience in accelerating body mri of pediatric patients,” in *Proceedings. IEEE International Symposium on Biomedical Imaging*, pp. 1039–1043, Dec. 2011.
- [50] E. Levine, B. Daniel, S. Vasanawala, B. Hargreaves, and M. Saranathan, “3d cartesian mri with compressed sensing and variable view sharing using complementary poisson-disc sampling,” *Magnetic Resonance in Medicine*, vol. 77, no. 5, pp. 1774–1785, 2017.
- [51] Y. Bliesener, S. G. Lingala, J. P. Haldar, and K. S. Nayak, “Impact of (k,t) sampling on dce mri tracer kinetic parameter estimation in digital reference objects,” *Magnetic Resonance in Medicine*, vol. 83, no. 5, pp. 1625–1639, 2020.
- [52] F. Wang, Z. Dong, T. G. Reese, B. Rosen, L. L. Wald, and K. Setsompop, “3d echo planar time-resolved imaging (3d-epTi) for ultrafast multi-parametric quantitative mri,” *NeuroImage*, vol. 250, p. 118963, 2022.
- [53] N. Wang, C. Liao, S. Srinivasan, X. Cao, J. Haldar, and K. Setsompop, “Circular echo-planar time-resolved imaging (cepti) for rapid time-resolved quantitative imaging,” in *Proceedings of ISMRM*, p. 761, 2022.

- [54] J. Yang, X.-X. Li, F. Liu, D. Nie, P. Lio, H. Qi, and D. Shen, “Fast multi-contrast mri acquisition by optimal sampling of information complementary to pre-acquired mri contrast,” *IEEE Transactions on Medical Imaging*, vol. 42, no. 5, pp. 1363–1373, 2023.
- [55] S. C. Deoni, B. K. Rutt, and T. M. Peters, “Rapid combined t1 and t2 mapping using gradient recalled acquisition in the steady state,” *Magnetic Resonance in Medicine*, vol. 49, no. 3, pp. 515–526, 2003.
- [56] E. M. Haacke, Y. Chen, D. Utriainen, B. Wu, Y. Wang, S. Xia, N. He, C. Zhang, X. Wang, M. M. Lagana, Y. Luo, A. Fatemi, S. Liu, S. Gharabaghi, D. Wu, S. K. Sethi, F. Huang, T. Sun, F. Qu, B. K. Yadav, X. Ma, Y. Bai, M. Wang, J. Cheng, and F. Yan, “Strategically acquired gradient echo (stage) imaging, part iii: Technical advances and clinical applications of a rapid multi-contrast multi-parametric brain imaging method,” *Magnetic Resonance Imaging*, vol. 65, pp. 15–26, 2020.
- [57] J. C. Ye, “Compressed sensing mri: a review from signal processing perspective,” *BMC Biomedical Engineering*, vol. 1, no. 8, pp. 2524–4426, 2019.
- [58] S. Blüml, L. R. Schad, B. Stepanow, and W. J. Lorenz, “Spin-lattice relaxation time measurement by means of a turboflash technique,” *Magnetic Resonance in Medicine*, vol. 30, no. 3, pp. 289–295, 1993.
- [59] M. J. Wainwright and M. I. Jordan, “Graphical models, exponential families, and variational inference,” *Foundations and Trends in Machine Learning*, vol. 1, Jan. 2008.
- [60] T. P. Minka and R. Picard, *A Family of Algorithms for Approximate Bayesian Inference*. PhD thesis, Massachusetts Institute of Technology, USA, 2001. AAI0803033.
- [61] M. Uecker, P. Lai, M. J. Murphy, P. Virtue, M. Elad, J. M. Pauly, S. S. Vasanawala, and M. Lustig, “Espirit—an eigenvalue approach to autocalibrating parallel mri: Where sense meets grappa,” *Magnetic Resonance in Medicine*, vol. 71, no. 3, pp. 990–1001, 2014.
- [62] E. Insko and L. Bolinger, “Mapping of the radiofrequency field,” *Journal of Magnetic Resonance, Series A*, vol. 103, no. 1, pp. 82–85, 1993.
- [63] A. Beck and M. Teboulle, “A fast iterative shrinkage-thresholding algorithm for linear inverse problems,” *SIAM Journal on Imaging Sciences*, vol. 2, no. 1, pp. 183–202, 2009.
- [64] S. Rangan, P. Schniter, and A. Fletcher, “On the convergence of approximate message passing with arbitrary matrices,” in *Proceedings of IEEE ISIT*, pp. 236–240, 2014.
- [65] C. Ghadery, L. Pirpamer, E. Hofer, C. Langkammer, K. Petrovic, M. Loitfelder, P. Schwingschuh, S. Seiler, M. Duering, E. Jouvent, H. Schmidt, F. Fazekas, J.-F. Mangin, H. Chabriat, M. Dichgans, S. Ropele, and R. Schmidt, “R2\* mapping for brain iron: associations with cognition in normal aging,” *Neurobiology of Aging*, vol. 36, no. 2, pp. 925–932, 2015.

- [66] J. H. O. Barbosa, A. C. Santos, V. Tumas, M. Liu, W. Zheng, E. M. Haacke, and C. E. G. Salmon, “Quantifying brain iron deposition in patients with parkinson’s disease using quantitative susceptibility mapping,  $r_2$  and  $r_2^*$ ,” *Magnetic Resonance Imaging*, vol. 33, no. 5, pp. 559–565, 2015.
- [67] J. Nocedal and S. J. Wright, *Numerical Optimization*. New York, NY, USA: Springer, 2006.



## Supporting Information

Additional Supporting Information may be found online in the Supporting Information section.

**Supporting Tables S1–S4** Retrospective undersampling with the variable-density pattern: normalized root mean square errors of recovered  $T_1$ ,  $R_2^*$  and proton density  $Z_0$  maps from the subjects at different sampling rates (10%, 15%, 20%). Three reconstruction approaches (LSQ, L1, AMP-PE) with four undersampling schemes (U1–U4) are compared in this table.

**Supporting Tables S5–S9** Retrospective undersampling with the Poisson-disk pattern: normalized root mean square errors of recovered  $T_1$ ,  $R_2^*$  and proton density  $Z_0$  maps from the subjects at different sampling rates (10%, 15%, 20%). Three reconstruction approaches (LSQ, L1, AMP-PE) with four undersampling schemes (U1–U4) are compared in this table.

**Supporting Table S10** Retrospective undersampling: normalized root mean square errors of recovered  $T_1$ ,  $R_2^*$  and proton density  $Z_0$  maps from the subject R1 at different sampling rates (10%, 15%, 20%). GraSP and AMP-PE were used as the reconstruction approaches under the U1 undersampling scheme with the variable-density (VD) pattern, and the central 10 axial slices were recovered.

**Supporting Figure S1** The factor graph of the sparse signal recovery task under the AMP framework: “○” represents the variable node, and “■” represents the factor node.

**Supporting Figures S2–S7** Retrospective undersampling with the variable-density pattern at the 15% and 20% undersampling rates: recovered  $T_1$ ,  $R_2^*$ , proton density maps and absolute error maps from the subject R1 using three reconstruction approaches (LSQ, L1, AMP-PE) and four undersampling schemes (U1–U4).

**Supporting Figures S8, S9** Prospective undersampling with the variable-density pattern at the 15% and 20% undersampling rates: recovered tissue parameters and absolute error maps from the subject P1 using two reconstruction approaches (L1, AMP-PE) and two undersampling schemes (U2, U4).

**Supporting Figures S10, S11, S12** Retrospective undersampling: recovered  $T_1$ ,  $R_2^*$ , proton density maps and absolute error maps from the subject R1 using the variable-density (VD) and Poisson-disk (PD) patterns at different sampling rates (10%, 15%, 20%). AMP-PE and U2 were chosen as the reconstruction approach and undersampling scheme respectively. When the sampling rate is 10%, VD achieved a lower NRMSE; when the sampling rates are 15% and 20%, PD achieved lower NRMSEs.

**Supporting Figures S13, S14** Retrospective undersampling with the variable-density pattern: recovered  $R_2^*$ , proton density maps and absolute error maps from the subject R1 using GraSP and AMP-PE approaches and U1 undersampling schemes. The recovered images by GraSP with 100 iterations have more errors than those with 10 iterations.